Timescales of successful and failed subduction: insights from numerical modelling

Authors: B. S. Knight[1,2*], J. H. Davies[2], F.A. Capitanio[1]

Affiliations:

[1] School of Earth, Atmosphere and Environment, Monash University, Melbourne

[2] School of Earth and Ocean Sciences, Cardiff University, Cardiff

Corresponding author: Ben Knight (ben.knight@monash.edu), +61 4910 92984

Accepted date: 25/08/20
Submitted date: 15/04/20

Abbreviated Title: Successful and failed subduction

Abstract

The relatively short duration of the early stages of subduction results in a poor geological record, limiting our understanding of this critical stage. Here, we utilize a 2D numerical model of incipient subduction, that is the stage after a plate margin has formed with a slab tip that extends to a shallow depth and address the conditions under which subduction continues or fails. We assess energy budgets during the evolution from incipient subduction to either a failed or successful state, showing how the growth of potential energy, and slab pull, is resisted by the viscous dissipation within the lithosphere and the mantle. The role of rheology is also investigated, as deformation mechanisms operating in the crust and mantle facilitate subduction. In all models, the onset of subduction is characterized by high lithospheric viscous dissipation and low convergence velocities, whilst successful subduction sees the mantle become the main area of viscous dissipation. In contrast, failed subduction is defined by the lithospheric viscous dissipation exceeding the lithospheric potential energy release rate and velocities tend towards zero. We show that development of a subduction zone depends on the convergence rate, required to overcome thermal diffusion and to localise deformation along the margin. The results propose a minimum convergence rate of ~ 0.5 cm yr^{-1} is required to reach a successful state, with 100 km of convergence over 20 Myr, emphasizing the critical role of the incipient stage.

Key words: Subduction zone processes, Rheology: mantle, Dynamics of lithosphere and mantle

1. Introduction

Subduction plays a key role in Earth's evolution as it provides the main driving force for plate motions, on-going deformation and the cycling of material in and out of the mantle [Forsyth and Uyeda, 1975]. The critical stages in the development of subduction zones are the initiation, where the plate margin is formed, and the incipient phase, where the slab tip extends to a shallow depth. This is followed by the lengthening of the slab at depth, until subduction eventually becomes self-sustaining. While self-sustained subduction has been subject of many studies [e.g. Conrad and Hager 1999; Funiciello et al. 2003; Billen and Hirth 2007; Capitanio et al. 2007; Capitanio et al. 2009; Schellart 2009; Garel et al. 2014], the incipient stage is poorly understood. This is partly because of the short duration of the incipient stage, and the record of this stage may be overprinted once the margin matures [Gurnis et al., 2004; Stern and Gerya, 2018]. This has hence made subduction initiation and the incipient stage, a difficult process to observe directly and therefore understand.

Subduction is the result of a gravitational instability, requiring two main conditions to occur: (1) deformation of the lithosphere to form a plate margin and (2) lengthening of the slab, to grow the gravitational instability and attain a self-sustaining state. Previous work addressing plate margin formation has focussed on the yield strength of lithosphere, which has to be overcome. The timescales for a new plate margin to form range from 2 to 5 Myr during forced convergence at pre-existing weaknesses [Hall et al., 2003; Gurnis et al., 2004] and may be aided by rapid plastic failure due to the addition of water and elasticity [Regenauer-Lieb et al., 2001]. Although very limited field data exists, observations from the Semail Ophiolite suggest subduction reached a self-sustaining state after ~ 8 Myr of forced convergence in the region [Guilmette et al., 2018].

Previous modelling studies, both numerical and analogue, have addressed subduction assuming an initial configuration with a slab extending to a depth of 100 to 250 km [e.g. Capitanio et al., 2010;

MacDougall et al., 2017; Agrusta et al., 2017] whilst force balance from McKenzie [1977] suggests a critical depth of 180 km for self-sustaining subduction at a minimum convergence rate of 1.3 cm yr^{-1}. Hall et al. [2003] and Gurnis et al. [2004] suggest 100 – 150 km of convergence is required along a fracture zone at a rate of ≥ 1 cm yr^{-1} to achieve self-sustaining subduction. Even with imposed boundary velocities, the growth of the instability is controlled by the deformation rate of the lithosphere and mantle. The slab begins to sink at low velocities initially, before exponentially increasing as resisting forces are overcome and slab pull becomes the dominant driving force, leading to self-sustaining subduction [Becker et al., 1999; Gurnis et al., 2004]. Additionally, the rheology of the surrounding mantle plays a role in the development of subduction zones, reducing the viscous drag at the slab edge [Gurnis et al., 2004; Billen and Hirth, 2005; Billen and Hirth, 2007; Jadamec, 2015]. Gurnis et al. [2004] showed that the strength of the mantle influences the evolution of the margin once the mantle viscosity exceeds 10^{20} Pa s, and only after the lithospheric strength has been overcome initially.

These studies suggest conditions for successful subduction, thereby defining the conditions under which subduction fails. To develop into a successful subduction margin, the negative buoyancy of the slab penetrating into the mantle must remain high enough to drive subduction. In a thermo-mechanic system, the nascent buoyancy force, during the incipient stage, may remain comparable or smaller than the resisting forces, resulting in a decrease of the deformation rate of the lithosphere and subduction velocity. Under these conditions, thermal diffusion is favoured and, as a consequence, the slab's temperature anomaly and its thermal buoyancy may vanish. This negative feedback may rapidly lead to subduction failure.

It is known that the evolution of subduction follows the balance of forces, with driving forces including slab pull (F_{SP}) and ridge push (F_{RP}), and induced mantle flow (F_S) [Baes and Sobolev, 2017; Baes et al., 2018]. Resisting forces include the slab strength, resulting in a resistance to bending prior to the trench (F_B), plate coupling at the plate boundary and its resistance to shearing (F_{PC}), the surrounding mantle's viscous resistance through drag (F_D) and by the amount of over-riding plate deformation (F_{OPD}) [McKenzie, 1977; Toth and Gurnis, 1998; Capitanio et al., 2007]. During incipient and self-sustaining subduction, the evolution of the slab is determined by the energy dissipation and its partitioning between the lithosphere and mantle. Previous studies, using both analogue and numerical modelling techniques, have illustrated how the energy in a subducting system is dissipated during self-sustaining subduction. Viscous dissipation in the lithosphere, as a percentage of the total energy, during self-sustaining subduction with no over-riding plate in both analogue and numerical models has been estimated to range from less than 20% [Stegman et al., 2006; Capitanio et al., 2007; Capitanio et al., 2009; Irvine and Schellart, 2012; Schellart, 2009] to around 50% [Buffett, 2006; Di Giuseppe et al., 2008] and up to as high as 95% [Conrad and Hager, 1999; Funiciello et al., 2003; Bellahsen et al., 2005]. A global reconstruction of energy dissipation at subduction zones by Stadler et al. [2010], estimated lithospheric dissipation at less than 25%, with the lithospheric component almost equally distributed between the weak zone and hinge region. Elasticity has been shown to maintain higher deformation rates during bending and retain slab strength during unbending but has minor effects on the overall morphology [Capitanio and Morra, 2012; Farrington et al., 2014].

This study investigates the evolution energy dissipation during the incipient subduction stage using a numerical model to determine the conditions for the growth of an incipient slab. The incipient stage is addressed here as the initial deformation phase that is focused within the lithosphere. In such a system, the deformation of the lithosphere must be overcome before the slab can lengthen and induce matle flow, which leads to self-sustaining, successful subduction. We investigate how the deformation is partitioned between the lithosphere and mantle during the incipient stage through viscous dissipation and define the timescale of the incipient stage. Additionally, key factors of the subduction system are addressed, such as rheology and plate ages, to assess their influence on the evolution from incipient subduction, to either a successful or failed state.

2. Model Overview

Thermomechanical models of subduction are performed using the code Fluidity, which uses a finite-element, control-volume method and an adaptive, unstructured discretization [e.g., Davies et al., 2007; 2008]. The model dimensions are 10,000 km by 2,900 km, with node spacing varied from 400 m to 200 km. The large dimensions reduce the influence of the boundary conditions [Enns et al., 2005; Chertova et al., 2012]. The higher resolution, which is driven by the adaptivity algorithm of Fluidity [Davies et al., 2011], is assigned to regions where variables experience a higher rate of change.

2.1 Governing equations and constitutive laws

We solve the conservation of mass, momentum and energy through the Boussinesq approximation of an incompressible Stokes fluid:

$$\partial_i u_i = 0, \tag{1}$$

$$\partial_i \sigma_{ij} = -\Delta\rho g_j, \tag{2}$$

$$\frac{\partial \mathrm{T}}{\partial \mathrm{t}} + u_i \partial_i T = \kappa \partial_i^2 T, \tag{3}$$

where u is the velocity vector and g is the acceleration due to gravity, σ_{ij} is the stress tensor due to strain rates. T is the temperature, κ the thermal diffusivity and $\Delta\rho$ is the density difference. The stress tensor, σ_{ij}, can be split into the deviatoric and lithostatic components:

$$\sigma_{ij} = \tau_{ij} - p\delta_{ij}, \tag{4}$$

where τ_{ij} is the deviatoric stress tensor, p is the dynamic pressure, and δ_{ij} is the Kronecker delta function. The deviatoric stress tensor and the strain rate tensor $\dot{\varepsilon}_{ij}$ are related by equation (5), where η is the viscosity and subscript *i* and *j* represent the vector direction.

$$\tau_{ij} = 2\eta\dot{\varepsilon}_{ij} = \left(\frac{\partial u_i}{\partial x_j} + \frac{\partial u_j}{\partial x_i}\right) \tag{5}$$

2.2 Rheology

The model incorporates a viscoplastic rheology, where the plastic rheology is implemented through yielding at low pressure and temperature through a brittle-failure type yield-stress law (eq. 6 and 7) while a viscous rheology is implemented through a stress - strain rate constitutive law for each creep mechanism (eq. 8). All values for the rheology are outlined in Table 1. The plastic rheology is determined by:

$$\eta_y = \frac{\tau_y}{2\dot{\varepsilon}_{\mathrm{II}}} \tag{6}$$

where η_y the yielding viscosity and $\dot{\varepsilon}_{II}$ the second invariant of the strain-rate tensor. τ_y, the yield strength, is calculated by:

$$\tau_y = \min(\tau_s + f_c P, \tau_{y,max}) \tag{7}$$

where τ_s is the surface yield strength, f_c is the friction coefficient, *P* is the lithostatic pressure and $\tau_{y,max}$ is the maximum yield strength. The values prescribed for the friction coefficient along the weak zone and within the model are consistent with previous values [e.g. Cattin et al., 1997; Iaffaldano, 2012; Arcay, 2012; Crameri et al., 2012; Crameri and Tackley, 2015]. Diffusion, dislocation and Peierls creep are determined by a constitutive law between stress and strain rate for each mechanism:

$$\eta_{diff/dis/P} = A^{-\frac{1}{n}}\exp\left(\frac{E+PV}{nRT_r}\right)\dot{\varepsilon}_{II}^{\frac{1-n}{n}} \tag{8}$$

where A is the prefactor, n is the stress component, E the activation energy and V the activation volume, P the lithostatic pressure ($=\rho_s gz$), R the gas constant. T_r is the temperature obtained by adding to the Boussinesq approximation an adiabatic gradient of 0.5 K/km in the upper mantle and 0.3 K/km in the lower mantle [Fowler, 2005].

The effective viscosity (η) is then evaluated for the entire domain through:

$$\eta = \left(\frac{1}{\eta_{diff}} + \frac{1}{\eta_{dis}} + \frac{1}{\eta_P} + \frac{1}{\eta_y}\right)^{-1} \tag{9}$$

Viscosity is capped in the model with a lower limit at 10^{18} Pa s, and upper limit of 10^{25} Pa s. Diffusion creep dominates lower mantle deformation, with a viscosity contrast of 30 between the upper and lower mantle, consistent with seismic observations [Karato et al., 1995].

A 5 km thick weak zone is situated along the top of the subducting slab that also follows the same rheological laws as the upper mantle, however a lower friction coefficient is prescribed, along with a viscosity cap of 10^{20} Pa s, ensuring decoupling between the two plates. The interface between the two plates is free to move in response to the dynamic evolution of the model. This weak zone simulates weak hydrated crust on the top of the subducting slab, a critical condition for subduction to occur [Crameri et al., 2012] and the rheology of the weak zone allows strain rate weakening to occur within the weak zone so strain can naturally localise. This weak zone is phased out below a depth of 200 km [Garel et al., 2014].

2.3 Model setup

The model setup (Fig. 1A) is derived from the work of Garel et al. [2014], with the initial bending angle (β) and radius of curvature modified to investigate the boundary between successful and failed subduction. No heat flux occurs on the side walls, whilst isothermal conditions are set on the top (T_s) and bottom (T_B) walls (T_s = 273 K, T_B = 1573 K). The model includes a free-slip boundary condition on the bottom and side walls, whilst a free surface is employed on the top surface to allow plate flexure in response to the underlying dynamics [Kramer et al., 2012].

The controlling parameter on the lithospheric strength is the temperature profiles of the subducting (SP) and over-riding plates (OP), dictated by the age-dependent thicknesses of the lithosphere. The thickness is determined via the half-space cooling model, where the age increases linearly from 0 Myr at the model boundary to the prescribed plate ages at the initial trench position at the centre of the domain (x^0_{trench} = 5,000 km). The initial temperature profile is thus determined by:

$$T(x,z,t=0) = T_s + (T_m - T_s)\mathrm{erf}\left(\frac{z}{2\sqrt{k\mathrm{Age}^0(x)}}\right) \tag{10}$$

where z is the depth, x the horizontal coordinate, t is the time, k is thermal diffusivity, T_s is the temperature at the surface and T_m the mantle temperature, with $Age^0(x)$ is the plates age at the given x coordinate.

We investigated cases with different initial thermal structures. These are defined by SP and OP ages at the trench. For each plate age combination, we also investigated varying the initial geometry of the subducting plate, by either changing the bending radius, or the initial bending angle β. The initial parameters for each case are listed in Table 2, where the case name includes the SP and OP age in Myr and if the case reaches a successful case. In addition, we have also tested the role of rheology by varying the deformation mechanisms operating within the lithosphere and mantle and also by investigating the strength of the weak zone.

2.4 Diagnostics

The initial depth below the surface of the subducting slab is defined as the deepest point of the subducting slab tip, as defined by the 1300 K isotherm (Fig. 1A). The 1300 K isotherm is considered the base of the lithosphere, where T > 1300 K is regarded as mantle. The horizontal plate velocity of the subducting (u_{SP}) and over-riding plate (u_{OP}) are measured at the surface where x = 2000 km and x = 8000 km, respectively. u_{SP} and u_{OP} are used to determine the convergence velocity ($u_x = u_{SP} + u_{OP}$), where trenchward motion is positive [Garel et al., 2014]. The slab tip velocity (u_T) is calculated from the deepest point available of the 1300 K temperature contour which denotes the subducting slab.

The energy dissipation in the system is measured by the viscous dissipation (VD) through internal deformation [Ranalli and Murphy, 1987; Conrad and Hager, 1999; Capitanio et al., 2007]. The viscous dissipation is calculated across the volume (v) of the lithosphere (OP & SP combined, ϕ_l^{VD}), where T < 1300 K, as well as the mantle (ϕ_m^{VD}), where T ≥ 1300 K. The sum of the two is the total viscous dissipation in the system $\phi_l^{VD} + \phi_m^{VD} = \phi_{TOT}^{VD}$:

$$\phi_{TOT}^{VD} = 4\int_V \eta \dot{\varepsilon}_{II} \dot{\varepsilon}_{II} \text{ dV} \tag{11}$$

The system is primarily driven by the potential energy (PE) of the subducting slab, along with a minor component of ridge push. Additional potential energy in the system arises from the temperature contrast between the asthenosphere and adiabatic mantle. These are quantified through the lithospheric ϕ_l^{PE} and mantle ϕ_m^{PE}, PE terms respectively, the sum of which is the total release rate of potential energy in the system $\phi_l^{PE} + \phi_m^{PE} = \phi_{TOT}^{PE}$, which is determined by:

$$\phi_{TOT}^{PE} = \int_V \rho_s g \alpha [T_m - T]\, u_y \; dV \tag{12}$$

Where ρ_s is the density at the surface, α is the thermal expansivity, T is temperature and T_m is the mantle temperature, with u_y representing the vertical velocity [Conrad and Hager, 1999].

We find that $\phi_{TOT}^{PE} \approx \phi_{TOT}^{VD}$, with minimal energy within the system lost due to the free surface implementation. The viscous dissipation and potential energy release rate are presented as a percentage of the total ($\phi^{VD} = \frac{\phi_l^{VD}}{\phi_{TOT}^{VD}}$, $\phi^{PE} = \frac{\phi_l^{PE}}{\phi_{TOT}^{PE}}$) where the absolute values of each vary as a function of time. It is important to note that a decrease in the lithospheric potential energy (ϕ_l^{PE}) over the total potential energy release rate in the system (ϕ_{TOT}^{PE}) is the consequence of thermal diffusion. This allows us to identify key information regarding the model, with viscous dissipation ϕ^{VD} used to identify the main area of resistance within the system, whilst the potential energy release rate ϕ^{PE} is used to determine how slab develops, whether it grows as the slab lengthens, or decreases as the slab thermally diffuses away.

Successful subduction is defined by the slab extending to mid upper-mantle depths and an increase in convergence and sinking velocities, which indicates vertical sinking of the slab as it over-comes lithospheric resistance. Failed subduction is identified through the vanishing of the slabs thermal signature and convergence velocities in the model declining toward zero, as the instability is unable to grow. Therefore, the combination of partitioning of energy within the system and convergence velocities best characterise incipient subduction. The incipient stage is characterised by high lithospheric viscous dissipation and low convergence velocities, which transitions to a decrease in lithospheric viscous dissipation and an increase in convergence velocity in the successful stage. In contrast, failed subduction is characterised by the proportion of lithospheric viscous dissipation exceeding the lithospheric potential energy release rate and convergence velocities tending towards zero.

3. Results

3.1 Energy and dissipation partitioning evolution

We assess the evolution of energy and its dissipation within the system over time to determine the transition between successful and failed subduction. In Table 2 we summarise the models' evolution indicating the conditions under which subduction is successful and any modifications to deformation mechanisms. The geometry and rheology of the slab are key components in the bouyancy-driven models.

To find the initial critical depth that results in successful subduction, we increased the depth of the slab tip (either through the bending radius or bending angle), to increase the slab pull force of the initial setup to facilitate subduction.

In case 20-100Y (Fig. 2A) the slab initially penetrates to a depth of 166 km. The lithospheric viscous dissipation ϕ^{VD} peaks at around 10 Myr at ~ 75%, which coincides with the lowest convergence (u_x) and vertical (u_y) velocities (Fig. 3A, 3C). ϕ^{VD} continues to decline to ~ 50% after 42.5 Myr. The potential energy release rate from the lithosphere ϕ^{PE} reaches ~ 75% at 20 Myr where it then remains constant for the rest of the evolution. As the model evolves the absolute values of both viscous dissipation (ϕ^{VD}_{TOT}) and potential energy release rate (ϕ^{PE}_{TOT}) increase, whilst ϕ^{VD} decreases due to a decrease in the proportion of lithospheric viscous dissipation (ϕ^{VD}_{l}) and an increase in proportion of mantle viscous dissipation (ϕ^{VD}_{m}) occurs as slabs sinking velocity increases after the incipient stage and reaches a successful state.

The slab in case 20-100N (Fig. 2B) initially extends to 141 km below the surface, leading to failed subduction, with ϕ^{VD} exceeding ϕ^{PE} around 10 Myr. ϕ^{PE} also decreases from > 80% to ~ 50% over 50 Myr, where the mantle component of potential energy release rate increases. In this case, the absolute values of both viscous dissipation and potential energy release rate decrease as the subduction zone fails, evident by velocities tending toward 0 cm yr^{-1} (Fig 3B, D).

Case 100-100Y represents a slab that initially extends to a depth of 162 km, with an older subducting plate (100 Myr) compared with case 20-100Y (20 Myr SP). The peak in ϕ^{VD}, at ~ 80%, occurs around 15 – 20 Myr, higher than any other successful case (Fig. 2C). However, the decline of ϕ^{VD} is faster than in case 20-100Y, resulting in a similar transition time from lithospheric to mantle dominated dissipation at ~ 42.5 Myr (Fig. 2A). ϕ^{PE} in case 100-100Y remains high at > 80%, as the slab lengthens

(Fig. 2C). During case 100-100N, which results in failed subduction, (Fig. 2D), ϕ^{VD} exceeds ϕ^{PE} at around 6 Myr, shorter than any other failed case.

The slab in case 100-20Y (Fig. 2E) initially extends to a depth of 162 km and is unique as it is the only case where lithospheric dissipation remains high, with ϕ^{VD} at ~ 70% throughout the evolution of the model, remaining in an incipient state for > 80 Myr. ϕ^{PE} remains high at ~ 80%, allowing subduction to continue, albeit at very low rates. In 100-20N, where subduction fails (Fig. 2F), the slab initially extends to a depth of 145 km, with ϕ^{VD} exceeding ϕ^{PE} after ~ 18 Myr.

Case 20-20Y (Fig. 2G) is also unique, as slab break-off is observed. ϕ^{VD} reaches a peak at around 10 Myr and then reaches the transition from lithosphere- to mantle-dominated viscous energy dissipation at around 17.5 Myr. ϕ^{VD} starts high at 60%, before decreasing to 10% at 22.5 Myr as the broken slab reaches a high vertical velocity (u_y, eq. 12, Fig. 3A) increasing strain rates in the mantle ($\dot{\varepsilon}_{II}$, eq. 11). The value of ϕ^{VD} then increases to 40% at 35 Myr as subduction continues, with ϕ^{VD} then decreasing to ~ 25% after 60 Myr as the slab reaches the 660 km transition zone. ϕ^{PE} follows a similar trend, where it decreases from > 80% to ~ 30% at 22.5 Myr during slab break-off, before increasing to 80% at 45 Myr as subduction continues. In case 20-20N (Fig. 2H), the slab initially extends to a depth of 141 km below the surface. In 20-20N, the instability is unable to grow, ultimately leading to the proportion of ϕ^{VD} exceeding ϕ^{PE} after ~ 10 Myr.

The slab in case 65-40Y (Fig. 2I) initially extends to a depth of 185 km. In case 65-40Y, Φ^{VD} reaches a peak between 10 - 15 Myr, before decreasing to ~ 40% after 27.5 Myr. The ϕ^{PE} in case 65-40Y remains relatively constant, at around 80% for the duration of the model. Velocities reach a minimum around 10-15 Myr, before increasing to 8 cm yr^{-1} at 27.5 Myr. Case 65-40N (Fig. 2J) initially extends to a depth of 154 km. ϕ^{VD} reaches a peak at 20 Myr, where it intersects with ϕ^{PE}. ϕ^{VD} exceeds ϕ^{PE} at around 22.5 Myr, resulting in failed subduction. As the slab is unable to lengthen, velocities tend toward 0 cm yr^{-1} (Fig. 3B, 3D).

In case 40-65Y (Fig. 2K), the slab tip initially extends to 150 km, with a peak in ϕ^{VD} observed at 10 – 15 Myr at ~ 70%. This peak corresponds to the lowest convergence velocity observed of 0.37 cm yr^{-1}. After the peak, ϕ^{VD} decreases to ~ 50 % and convergence velocity increases to 1.9 cm yr^{-1} at 37.5 Myr. ϕ^{PE} remains high, at ~ 80% for the entire evolution. In case 40-65N, ϕ^{VD} exceeds ϕ^{PE} at ~ 12 Myr (Fig. 2L), whilst velocities decrease from ~ 0.5 cm yr^{-1} initially to 0 cm yr^{-1} after 25 Myr (Fig. 3B, 3D), resulting in failed subduction.

3.2 Role of Rheology

The rheology of the model is a key parameter, as it changes the viscous resistance and therefore the dissipation partitioning within the domain. The previous models, with all deformation mechanisms active, are all able to subduct when the slab tip extends to a depth of 150 - 160 km into the mantle (Table 2), with the initial geometry providing the required potential energy to over-come resistive forces at work. As the critical depth is determined by the resistive forces, we also examined two additional setups that modified (1) the weak zone decoupling between the subducting and over-riding plate and (2) the removal of deformation mechanisms operating in the model. Removing deformation mechanisms alters the strength of the lithosphere and mantle (Fig. 1C), allowing an assessment of the key deformation mechanisms and key areas of deformation within the system.

We find that increasing the coupling between the subducting and over-riding plate, by increasing the viscosity cap of the weak layer, requires an increase in the initial slab depth, suggesting the fault interface along convergent margins can inhibit subduction. The required depth of the slab tip for subduction to develop increases from 125 km (case LS-20-100Y-150) at a viscosity cap of 5 x 10^{19} Pa s to 166 km at 1 x 10^{20} Pa s (case 20-100Y); at 3 x 10^{20} Pa s (case HS-20-100N-225) subduction is unable to become successful even when the initial slab extends to a depth of ~ 200 km. The results show that the initial potential energy required increases due to an increase in strength of the plate interface, however the maximum duration of the incipient stage remains consistent at < 20 Myr (Fig. 4).

The role of deformation mechanisms is also investigated by removing: (i) Peierls mechanism, which operates at higher temperatures than yielding within the slab, reducing the slab's strength and resistance to bending and stretching. (ii) Dislocation creep, which mainly occurs around the slab edges, reducing the mantle strength and thus the drag resistance as the slab subducts. To remove each mechanism, the prefactor for each was modified (Table 1). Both changes in rheology resulted in an increase in the initial slab tip depth required for successful subduction to occur.

The removal of dislocation creep results in failed subduction in all cases tested, as the slab is unable to lengthen due to a mantle viscosity of ~10^{21} Pa s. This results in diffusion of the slab as no new cold material is advected into the subduction zone. The removal of Peierls creep in NP65-40Y-250 results in successful subduction (Fig. 5) when the slab tip is initially at a depth of 220 km. Both cases NP-65-40Y-250 and NP-65-40Y-275 transition to a successful state early, at around 3 Myr, whilst in NP-65-40N-250, ϕ^{VD} increases above ϕ^{PE} around 17 Myr (Fig. 5). The results show that the duration of the incipient stage remains consistent regardless of rheology due to thermal diffusion of the slab, with a maximum duration of 20 Myr.

4. Discussion

4.1 The role of viscous dissipation in incipient subduction

The energy partitioning during incipient subduction varies greatly over time as the model evolves and the key areas of deformation differs compared to steady-state, successful subduction. The evolution of viscous dissipation over time shows that, in all subducting cases (Fig. 2), the lithosphere (ϕ^{VD}) initially accounts for around 60% of the energy dissipated in the system. This increases in the early stages of incipient subduction, where the proportion of lithospheric dissipation (ϕ^{VD}) grows to a maximum of ~80%, which is less than the highest estimates of ~ 95% during steady-state subduction [Conrad and Hager, 1999; Funiciello et al., 2003; Bellahsen et al., 2005]. This peak in ϕ^{VD} corresponds to the minimum convergent and slab sinking velocities experienced in the model during its evolution. Although both ϕ_l^{VD} and ϕ_m^{VD} decrease with decreasing velocity during this stage, ϕ_m^{VD} decreases at a faster rate proportionately as the lithosphere is undergoing internal deformation, increasing ϕ^{VD} [Capitanio et al., 2007]. This is a consequence of the need to initially overcome the lithospheric strength, which then allows the instability to grow subsequently. Once the lithosphere has been sufficiently deformed, ϕ^{VD} begins to decrease and subduction velocities increase. ϕ_l^{PE} then increases as the instability grows, whilst ϕ^{PE} remains constant at ~ 80% as both ϕ_l^{PE} and ϕ_m^{PE} grow proportionally. This critical point, where subduction velocities can now increase and ϕ^{VD}decreases, defines the point at which subduction has reached a successful state. This is also observed in other studies, where the peak in the force required to form a subduction zone is due to overcoming lithospheric resistance [Hall et al., 2003], with an increase in plate age requiring a larger force for subduction to initiate [Gurnis et al., 2004].

In the majority of cases, ϕ^{VD}then decreases to < 50% as the mantle becomes the main area of deformation and energy dissipation, in agreement with the lithospheric dissipation values of 35% to 50% observed by Di Giuseppe et al., [2008]. This highlights the decreasing proportion of energy dissipated within the lithosphere as subduction evolves [Gerardi et al., 2019]. However, as the majority of cases have not yet reached a steady-state, due to increasing subduction velocities, values of ~ 35% [Capitanio et al., 2007; Gerardi et al., 2019] or as low as < 20% could be reached [e.g. Schellart, 2009; Stegman et al., 2006; Capitanio et al., 2009; Stadler et al., 2010]. Values of ~ 25% observed in 20-20Y as the slab reaches the 660 km transition zone after 60 Myr. However, one case, 100-20Y, shows a sustained high value of ϕ^{VD}

at around 75% for ~ 90 Myr. But, as ϕ^{VD} remains below ϕ^{PE} (Fig. 2E) and the convergence velocity remains high enough, the slabs thermal signature does not diffuse away (Fig. 7A) and subduction continues at a very low rate (Fig. 3A, 3C). Whilst the nature of subduction zones are three-dimensional and the evolution is influenced by toroidal and poloidal flow, the partitioning of energy observed here is similar to 3D models [Stegman et al., 2006], suggesting that the poloidal flow in two-dimension encapsulates the dissipation of potential energy within the system.

4.2 Slab break-off

Slab break-off is observed in 20-20Y (Fig. 6A-B), where the initial rapid acceleration of the subducting slab results in stretching and break-off within 20 Myr (Fig 3A, C). During the evolution of 20-20Y, an initial reduction of viscosity in the slab's core is seen at a depth of around 100 km after 6.4 Myr, where the transition from dislocation to Peierls creep is observed (Fig. 6A-B), whilst thinning of the 1300 K isotherm begins at around 15 Myr. The slab continues to stretch at the necking point, ultimately leading to slab break-off at around 19 Myr (Fig. 6A, 6B).

The slab break-off duration observed here is defined as the duration between the onset of visual necking and complete break-off and occurs over very short periods of time (< 5 Myr) with viscous creep being the dominant deformation mechanism enabling slab break-off (Fig. 6B) in agreement with Duretz et al. [2012]. However, a reduction in viscosity is first observed at 6 Myr, with a time of ~ 13 Myr between the onset of weakening and slab break-off. This suggests that the initial weakening, beginning the slab break-off process, occurs much earlier than visible necking of the slab, suggesting the duration over which slab break-off occurs may be longer than previously thought (Fig. 6A, 6B). However, the duration of slab break-off may be shortened by additional mechanisms, including shear heating [Duretz et al., 2012], grain size reduction [Bercovici et al., 2015] or through strain weakening that records deformation history.

The sinking of the detached slab has a two-fold effect: (1) it reduces the viscosity of the mantle through induced strain rates, and (2) it propagates viscous stress, i.e. suction [Baes and Sobolev, 2017; Baes et al., 2018] aiding the continuation of subduction of the remaining slab. This suction force is less than the slab pull, but still aids subduction. The detached slab's thermal signature eventually diffuses away after ~ 27 Myr and subduction of the remaining slab continues. This is observed in an increase in u_y and u_x after ~ 27 Myr until 45 Myr, where velocities begin to decrease as the subducting slab reaches the upper-lower mantle boundary (Fig. 3A, 3C).

The weak subducting and over-riding plate in case 20-20Y allows the lithospheric resistance to be easily overcome, resulting in high initial plate velocities (Fig. 3A, 3C). This produces high induced strain rates, reducing the viscosity (Fig. 6), in both the subducting plate, due to bending, and the over-riding plate, due to stretching caused by trench motion, allowing the slab to sink faster when compared with a stronger, thicker over-riding plate, in agreement with previous studies [Yamato et al., 2009; Capitanio et al., 2010; Butterworth et al., 2012]. In case 20-20Y, slab tip velocities (Fig. 3A) are higher than the convergence velocities, i.e. $u_y > u_x$, (Fig. 3C), suggesting the stresses do not fully propagate to the surface, due to tension and stretching of the slab near the surface [Davies and von Blanckenburg, 1995; Gerya et al., 2004]. However, the absolute surface velocities (u_x, Fig. 3A) are low, with the anomalously high tip velocities (u_y, Fig. 3C) arising from the broken slab, suggesting that thermal weakening of the slab [e.g. Duretz et al., 2012; van Hunen and Allen, 2011] at a low Peclet number [Boutelier and Cruden, 2017] aids the slab break-off process. Slab break-off is further aided by a reduction of viscous support of the subducting slab through viscous creep deformation in the mantle (Fig. 6), consistent with previous models [e.g. Gerya et al., 2004; Burkett and Gurnis, 2012]. The plate kinematics and resulting feedback mechanisms, caused by high temperatures around the slab due to the young over-riding plate, results in viscous creep reducing the viscous support of the subducting slab from the surrounding mantle and increased amounts of deformation at the necking point, leading to slab break-off to occur in case 20-20Y after 19 Myr.

4.3 Constraints on incipient subduction timescales

Our models provide a way to estimate the timescales of incipient subduction, when lithospheric deformation is highest [Gurnis et al., 2004]. The incipient stage is defined as the time until the peak in ϕ^{VD} and subduction velocities are at a minimum. The duration of the incipient stage is < 20 Myr, in agreement with previous estimates on subduction initiation from a range of convergent margins, which are estimated at ~10 Myr by Becker et al. [1999], 15 Myr [Faccenna et al., 1999] and up to 20 Myr [Nikolaeva et al., 2010]. Our models, with all deformation mechanisms active, also agree with critical depths that have been suggested in the literature, ranging from 100 – 150 km [Hall et al., 2003; Gurnis et al., 2004] and up to 180 km [McKenzie, 1977].

We find that the age of the subducting plate plays a relevant role in the evolution of incipient subduction margins, whereby increasing the subducting plate age increases the strength of the plate, restricting the bending of the slab. This leads to a longer duration of the incipient stage, where the transition to successful subduction is observed through the ϕ^{VD} peak at ~ 10 Myr and ~ 20 Myr in case 20-100Y (Fig. 2A) and case 100-100Y (Fig. 2C), respectively. This is in agreement with subduction initiation being easier at younger margins as the younger plate requires less force to deform and form the margin [Gurnis et al., 2004; Zhong and Li, 2019].

The role of the over-riding plate in facilitating incipient subduction is also important. A young over-riding plate can accommodate convergence to allow subduction to occur. This is observed in case 100-20Y, with an old subducting plate (100 Myr) and young over-riding plate (20 Myr). In this subducting case, no transition from incipient to successful subduction is observed, with ϕ^{VD} remaining high at ~70% after 80 Myr (Fig. 2E). During the evolution of case 100-20Y, the OP deforms largely as convergence is ongoing (Fig. 7A), with the high ϕ^{VD} keeping the convergence velocity low. The velocities from the model (Fig. 3C) suggest that stretching of the over-riding plate is facilitating the majority of convergence (Fig. 7A, 7B). The strength of a viscous fluid is very different between bending and extension. During extension, resistance to stretching is proportional to the product of effective viscosity and thickness [Turcotte and Schubert, 2002; Capitanio et al., 2007; Garel et al., 2014] while resistance to bending is proportional to the product of effective viscosity and the cube of the thickness [Turcotte and Schubert, 2002; Ribe, 2001; Capitanio et al., 2007; Garel et al., 2014]. This may be occurring in 100-20Y, where stretching and deformation of the weak over-riding plate facilitates subduction instead of deformation of the subducting plate, limiting the convergence velocity and the advection rate.

The evolution of case 100-20Y, where a weak over-riding plate accommodates the majority of trench motions, suggests that the over-riding plate is an important area of viscous dissipation in the incipient stage, and may be higher than the 0.4% previously suggested during steady-state subduction [Chen et al., 2015]. The slab extends to a depth of ~ 600 km, with ~ 400 km of slab roll-back from the initial trench position, with convergence velocities (u_x) of ~ 0.5 cm yr^{-1} (Fig. 3C). This suggests subduction can remain in an ongoing, incipient state for long periods. Subduction is actively on-going in case 100-20Y through the lengthening of the slab and penetration into the upper mantle (Fig. 7A-B), where subduction is possible with sustained convergence velocities of ~ 0.5 cm yr^{-1} (Fig. 3A, 3C). This implies a minimum of ~ 100 km of convergence within 20 Myr for subduction to occur, in agreement with previous studies [Hall et al., 2003; Gurnis et al., 2004]

The failed subduction cases also provide insight into the incipient stage, suggesting that if convergence velocities remain low (< 0.5 cm yr^{-1}), the subducting slab will begin to lose buoyancy due to thermal diffusion, resulting in a further decline in convergence velocity. This leads to less potential energy being released in the system due to its dependence on the slab sinking velocity, u_y (eq. 12). This negative feedback ultimately leads to failed subduction. In all failed subduction cases (Fig. 2), the lithospheric viscous dissipation exceeds the lithospheric potential energy release rate early in the evolution, between 8 - 22 Myr. Peaks in the lithospheric dissipation are up to 85% in some cases. The high lithospheric dissipation prevents the instability to grow (Fig. 2) and therefore reduces the advection of cold material into the subduction zone. This allows thermal diffusion from the hot mantle to heat up the subducting slab's negative thermal anomaly and therefore subduction fails as the driving force disappears.

4.4 Rheology controls on incipient subduction

The weak zone, at the interface between the subducting and over-riding plate, is a key component required for successful subduction, as an increase in strength increases the plate coupling, resisting the lengthening of the slab length. The weak zone makes a negligible contribution to the lithospheric viscous dissipation throughout the system's evolution if it is weak enough. However, the weak zone can become an important area of dissipation with increasing strength [Conrad and Hager 1999] and may even dissipate similar amounts of energy as the bending zone during steady-state subduction [Stadler et al., 2011]. Our models show that with increasing strength, the influence of the plate interface on subduction and energy dissipation increases. This implies sufficient decoupling is required between the plates, with increasing strength requiring an increase in the initial amount of potential energy. An increase in viscosity from 5 x 10^{19} Pa s (case LS-20-100Y-150) to 1 x 10^{20} Pa s (case 20-100Y) increases the required initial slab tip depth for successful subduction by ~ 41 km (125 km to 166 km, respectively). This implies a greater initial potential energy is required for successful subduction, when only the weak zone strength is modified, illustrating the role of the plate interface rheology.

From Fig. 4, different timescales of incipient subduction can be seen based on the initial bending radius, and thus depth. This demonstrates the longer the initial slab, the higher the initial potential energy and the quicker the slab can overcome the lithospheric resistance and accelerate, decreasing the time to transition from incipient to successful subduction. This is seen in case LS-20-100Y-200 where the lithospheric viscous dissipation peaks after 9 Myr, whilst LS-20-100Y-150 peaks at ~15 Myr.

Effectively removing dislocation creep in the upper mantle highlights the role of mantle drag. This results in diffusion creep becoming the dominant deformation mechanism in the mantle, with a mantle viscosity of $\sim 10^{21}$ Pa s. Diffusion creep around the slab edge is unable to reduce the resistive drag force from the mantle as it cannot reduce the viscosity of the surrounding mantle around the slab as effectively as dislocation creep. Elasticity, although not included here, also influences the evolution of subduction zones. It has been shown to maintain higher deformation rates during bending and retain slab strength during unbending, but has minor effects on the overall morphology [Capitanio and Morra, 2012; Farrington et al., 2014].

The removal of Peierls mechanism highlights the role of the strength of the slab. In case NP-65-40Y-250, yielding of the slab is able to facilitate some deformation and reduce the viscosity of the slab. However, yielding is not as efficient as Peierls mechanism at reducing the viscosity in those regions, increasing the amount of potential energy required to reach successful subduction. However, the duration of the incipient stage remains consistent at < 20 Myr (Fig. 5).

The variations in rheology investigated here suggests that both lithospheric and mantle deformation are key components for successful subduction to occur, similar to observations by Jadamec [2015]. In all cases that evolve successfully, the transition from incipient to successful subduction varies in time, but are all within 20 Myr. The model's initial bending radius and rheology can alter the evolution, with an increase in the length of slab increases the slabs potential energy, decreasing the duration of the incipient stage. However, if the lithospheric strength cannot be over-come and the instability cannot grow within 20 Myr, the slab thermally diffuses away and subduction fails, regardless of the local conditions.

4.5 Topography constraints on incipient subduction

The free surface in the model allows an assessment of the topography at convergent zones during incipient subduction. As the topography is the surface expression of large-scale geodynamic processes, this allows a first-order comparison between incipient subduction zones and the model evolution [Crameri et al., 2017].

Each case has a unique topographic evolution, providing useful diagnostics. However, there are common features across all successful cases. During the incipient stage, the subduction zones are characterised by: (1) an area of subsidence in the bending region of the subducting slab up to 200 km wide and (2) subsidence in the over-riding plate due to slab roll-back, or a back-arc depression (Fig. 8A), as illustrated by Crameri et al. [2017]. Successful subduction is characterised by additional features (Fig. 8C), including: (1) the formation of a fore-bulge, with uplift in the "outer-rise" up to 200 m above the original free surface, (2) the presence of an extensional basin where the main area of slab bending is occurring, (3) a trench up to 6 km deep, similar to topography in Toth and Gurnis [1998]. Most cases also show an area of uplift in the over-riding plate prior to the back-arc depression, similar in appearance to an island arc [Crameri et al., 2017]. In failed cases, these features do not develop and only a proto-trench, where the initial perturbation was present, is visible, at < 4 km deep, that narrows as subduction ceases in the region (Fig. 8B, 8D).

These results allow a direct comparison with topography in nature. Although lack of extensive observations prevents a thorough comparison, our work is compatible with reported cases. The Vitiaz trench, as discussed by Gurnis et al. [2004] is a fossil subduction zone, where subduction ceased ~ 10 Ma. The topography at the Vitiaz trench (VT) is very similar to that seen in the failed subduction cases, where the trench is still visible as a depression in the surface (Fig. 9B), however it is not as deep (~1 km), as surrounding active subduction zones, such as the New Hebrides trench (NHT) (Fig. 9B). The topography of the NHT shows the same features observed in successful subduction cases, with uplift in the fore-bulge and island-arc region either side of the trench, as well as some subsidence in the active bending area.

In comparison, the Macquarie Ridge Complex, off of the southwest coast of New Zealand, was defined by Gurnis et al. [2004] as a 'forced' subduction zone. Topography shows (1) a well-defined trench ~30 km wide, the Puysegur Trench; (2) uplift in the back-arc region, the Puysegur ridge and (3) development of a trough between 10 km to 40 km wide on the over-riding plate between 47°S and 48°S (Fig. 9A), indicative of slab roll-back occurring in that region. There is also some subsidence prior to the trench, however it is not as well defined as subsidence in the NHT, and no fore-bulge is observed in the topography. Although the area is complicated by oblique convergence, the topography in the region suggests that the Macquarie Ridge Complex could be considered to have reached a self-sustaining, successful state in some areas.

5. Conclusions

We have studied the incipient stage of subduction within a thermomechanical system through the evolution of a short slab into a fully self-sustained subduction in the upper mantle. During incipient subduction, the available forces are accommodated mostly by internal deformation of the down-going and over-riding plate. This inhibits subduction development, which slows down slab velocities and causes diffusion of the slab's thermal buoyancy, further decreasing driving forces. This negative feedback may ultimately lead to subduction failure. We assess the evolution of this stage through energy dissipation and find that the critical time for subduction to develop from incipient to successful subduction is < 20 Myr, with average instability growth rates of ≥ 0.5 cm yr^{-1}, resulting in a minimum of 100 km of convergence required. In all failed cases, we observe the lithospheric viscous dissipation (ϕ^{VD}) exceeding the lithospheres potential energy release rate (ϕ^{PE}) early in the evolution, < 20 Myr, ceasing subduction due to a lack of driving forces caused by thermal diffusion of the slab.

The incipient phase is characterised by low convergence velocities and a high proportion of lithospheric dissipation of available potential energy. The age of the over-riding plate influences the duration of the incipient stage. Increasing the age of the over-riding plate decreases plate velocities, as they are rigid, restricting trench motion. Young over-riding plates increase trench motion; however, they can also hinder subduction velocities in extreme cases. A young over-riding plate can accommodate the majority of deformation through stretching, whilst the subducting plate remains relatively less deformed and unable to subduct freely, resulting in low convergence rates and a slow evolution of the margin.

The rheology of both the mantle and lithosphere also influence the dissipation partitioning and, therefore, the incipient subduction stage. In the lithosphere, yielding and Peierls creep critically decrease the resistance to bending at the hinge, key area of deformation required to reach a successful state. In the mantle, dislocation creep, driven by slab-induced flow, allows sufficient deformation around the slab to reduce drag resistance. Without these mechanisms operating, a significant increase in the amount of potential energy is required to reach a successful state. Similarly, an increase in the strength of the subduction zone interface, increasing the inter-plate coupling, requires a larger initial potential energy. These results highlight the key areas of deformation which are required to reach a successful state.

The models show distinctive topographic evolution, allowing a clear discrimination between successful and failed subduction. Although the record of failed subduction is scarce, a comparison between reported observed cases and models provides a positive match, showing insights in a process that might be relatively poorly represented, yet important for our understanding of subduction zone dynamics.

5. Acknowledgments

This research was partly supported by *Australian Research Council Future Fellowship* FT170100254 awarded to F.A.C. This research has benefitted from the research funded by Natural Environment Research Council NE/M000397/1, NE/I024429/1 awarded to JHD. The simulations benefitted from using Supercomputing Wales, and the support and facilities of the Advanced Research Computing at Cardiff (ARCCA) division located at Cardiff University. BK acknowledges the support, provided by the School of Earth and Ocean Sciences at Cardiff University, related to the MESci Project module, where this work was started. We acknowledge the very valuable comments of Mike Gurnis and previous reviewers.

6. Reference List

Agrusta, R., Goes, S., & van Hunen, J. (2017). Subducting-slab transition-zone interaction: Stagnation, penetration and mode switches. *Earth and Planetary Science Letters*, *464*, 10–23. https://doi.org/10.1016/j.epsl.2017.02.005

Amante, C. & Eakins, B.W. (2009). ETOPO1 1 Arc-Minute Global Relief Model: Procedures, Data Sources and Analysis. NOAA Technical Memorandum NESDIS NGDC-24. National Geophysical Data Center, NOAA.

Arcay, D. (2012). Dynamics of interplate domain in subduction zones: influence of rheological parameters and subducting plate age. *Solid Earth*, *3*(2), 467–488. https://doi.org/10.5194/se-3-467-2012

Baes, M., & Sobolev, S. V. (2017). Mantle Flow as a Trigger for Subduction Initiation: A Missing Element of the Wilson Cycle Concept. *Geochemistry, Geophysics, Geosystems*, *18*(12), 4469–4486. https://doi.org/10.1002/2017GC006962

Baes, M., Sobolev, S. V., & Quinteros, J. (2018). Subduction initiation in mid-ocean induced by mantle suction flow. *Geophysical Journal International*, *215*(3), 1515–1522. https://doi.org/10.1093/gji/ggy335

Becker, T. W., Faccenna, C., O'Connell, R. J., & Giardini, D. (1999). The development of slabs in the upper mantle: Insights from numerical and laboratory experiments. *Journal of Geophysical Research: Solid Earth*, *104*(B7), 15207–15226. https://doi.org/10.1029/1999JB900140

Bellahsen, N., Faccenna, C., & Funiciello, F. (2005). Dynamics of subduction and plate motion in laboratory experiments: Insights into the "plate tectonics" behavior of the Earth. *Journal of Geophysical Research: Solid Earth*, *110*(B1). https://doi.org/10.1029/2004JB002999

Bercovici, D., Schubert, G., & Ricard, Y. (2015). Abrupt tectonics and rapid slab detachment with grain damage. *Proceedings of the National Academy of Sciences*, *112*(5), 1287–1291. https://doi.org/10.1073/pnas.1415473112

Billen, M. I., & Hirth, G. (2005). Newtonian versus non-Newtonian upper mantle viscosity: Implications for subduction initiation. *Geophysical Research Letters*, *32*(19), n/a-n/a. https://doi.org/10.1029/2005GL023457

Billen, M. I., & Hirth, G. (2007). Rheologic controls on slab dynamics. *Geochemistry, Geophysics, Geosystems*, *8*(8), n/a-n/a. https://doi.org/10.1029/2007GC001597

Boutelier, D., & Cruden, A. R. (2017). Slab breakoff: Insights from 3D thermo-mechanical analogue modelling experiments. *Tectonophysics*, *694*, 197–213. https://doi.org/10.1016/j.tecto.2016.10.020

Buffett, B. A. (2006). Plate force due to bending at subduction zones. *Journal of Geophysical Research*, *111*(B9). https://doi.org/10.1029/2006JB004295

Burkett, E., & Gurnis, M. (2013). Stalled slab dynamics. *Lithosphere*, *5*(1), 92–97. https://doi.org/10.1130/L249.1

Butterworth, N. P., Quevedo, L., Morra, G., & Müller, R. D. (2012). Influence of overriding plate geometry and rheology on subduction. *Geochemistry, Geophysics, Geosystems*, *13*(6), n/a-n/a. https://doi.org/10.1029/2011GC003968

Byerlee, J. (1978). Friction of rocks. *Pure and Applied Geophysics*, *116*(4), 615–626. https://doi.org/10.1007/BF00876528

Capitanio, F. A., & Morra, G. (2012). The bending mechanics in a dynamic subduction system: Constraints from numerical modelling and global compilation analysis. *Tectonophysics*, *522–523*, 224–234. https://doi.org/10.1016/j.tecto.2011.12.003

Capitanio, F. A., Morra, G., & Goes, S. (2009). Dynamics of plate bending at the trench and slab-plate coupling. *Geochemistry, Geophysics, Geosystems*, *10*(4), n/a-n/a. https://doi.org/10.1029/2008GC002348

Capitanio, F. A., Stegman, D. R., Moresi, L. N., & Sharples, W. (2010). Upper plate controls on deep subduction, trench migrations and deformations at convergent margins. *Tectonophysics*, *483*(1–2), 80–92. https://doi.org/10.1016/j.tecto.2009.08.020

Capitanio, F., Morra, G., & Goes, S. (2007). Dynamic models of downgoing plate-buoyancy driven subduction: Subduction motions and energy dissipation. *Earth and Planetary Science Letters*, *262*(1–2), 284–297. https://doi.org/10.1016/j.epsl.2007.07.039

Cattin, R., Lyon-Caen, H., & Chéry, J. (1997). Quantification of interplate coupling in subduction zones and forearc topography. *Geophysical Research Letters*, *24*(13), 1563–1566. https://doi.org/10.1029/97GL01550

Chen, Z., Schellart, W. P., & Duarte, J. C. (2015). Quantifying the energy dissipation of overriding plate deformation in three-dimensional subduction models: Overriding plate energy dissipation. *Journal of Geophysical Research: Solid Earth*, *120*(1), 519–536. https://doi.org/10.1002/2014JB011419

Chertova, M. V., Geenen, T., van den Berg, A., & Spakman, W. (2012). Using open sidewalls for modelling self-consistent lithosphere subduction dynamics. *Solid Earth*, *3*(2), 313–326. https://doi.org/10.5194/se-3-313-2012

Conrad, C. P., & Hager, B. H. (1999). Effects of plate bending and fault strength at subduction zones on plate dynamics. *Journal of Geophysical Research: Solid Earth*, *104*(B8), 17551–17571. https://doi.org/10.1029/1999JB900149

Crameri, F. & Tackley, P. J. (2015). Parameters controlling dynamically self-consistent plate tectonics and single-sided subduction in global models of mantle convection. *Journal of Geophysical Research: Solid Earth*, *120*(5), 3680–3706. https://doi.org/10.1002/2014JB011664

Crameri, F., Lithgow-Bertelloni, C. R., & Tackley, P. J. (2017). The dynamical control of subduction parameters on surface topography. *Geochemistry, Geophysics, Geosystems*, *18*(4), 1661–1687. https://doi.org/10.1002/2017GC006821

Crameri, F., Tackley, P. J., Meilick, I., Gerya, T. V., & Kaus, B. J. P. (2012). A free plate surface and weak oceanic crust produce single-sided subduction on Earth. *Geophysical Research Letters*, *39*(3), n/a-n/a. https://doi.org/10.1029/2011GL050046

Davies, D. R., Davies, J. H., Hassan, O., Morgan, K., & Nithiarasu, P. (2007). Investigations into the applicability of adaptive finite element methods to two-dimensional infinite Prandtl number thermal and thermochemical convection. *Geochemistry, Geophysics, Geosystems*, *8*(5), n/a-n/a. https://doi.org/10.1029/2006GC001470

Davies, D.R., Davies, J. H., Hassan, O., Morgan, K., & Nithiarasu, P. (2008). Adaptive finite element methods in geodynamics: Convection dominated mid-ocean ridge and subduction zone simulations. *International Journal of Numerical Methods for Heat & Fluid Flow*, *18*(7/8), 1015–1035. https://doi.org/10.1108/09615530810899079

Davies, D.R., Wilson, C.R. and Kramer, S.C. (2011). Fluidity: A fully unstructured anisotropic adaptive mesh computational modeling framework for geodynamics. *Geochemistry, Geophysics, Geosystems* **12**(6). doi: https://doi.org/10.1029/2011GC003551.

Davies, J. H., & von Blanckenburg, F. (1995). Slab breakoff: A model of lithosphere detachment and its test in the magmatism and deformation of collisional orogens. *Earth and Planetary Science Letters*, *129*(1), 85–102. https://doi.org/10.1016/0012-821X(94)00237-S

Di Giuseppe, E., van Hunen, J., Funiciello, F., Faccenna, C., & Giardini, D. (2008). Slab stiffness control of trench motion: Insights from numerical models. *Geochemistry, Geophysics, Geosystems*, *9*(2), n/a-n/a. https://doi.org/10.1029/2007GC001776

Duretz, T., Schmalholz, S. M., & Gerya, T. V. (2012). Dynamics of slab detachment. *Geochemistry, Geophysics, Geosystems*, *13*(3). https://doi.org/10.1029/2011GC004024

Enns, A., Becker, T. W., & Schmeling, H. (2005). The dynamics of subduction and trench migration for viscosity stratification. *Geophysical Journal International*, *160*(2), 761–775. https://doi.org/10.1111/j.1365-246X.2005.02519.x

Faccenna, C., Giardini, D., Davy, P., & Argentieri, A. (1999). Initiation of subduction at Atlantic-type margins: Insights from laboratory experiments. *Journal of Geophysical Research: Solid Earth*, *104*(B2), 2749–2766. https://doi.org/10.1029/1998JB900072

Farrington, R. J., Moresi, L.-N., & Capitanio, F. A. (2014). The role of viscoelasticity in subducting plates. *Geochemistry, Geophysics, Geosystems*, *15*(11), 4291–4304. https://doi.org/10.1002/2014GC005507

Forsyth, D., & Uyeda, S. (1975). On the Relative Importance of the Driving Forces of Plate Motion. *Geophysical Journal International*, *43*(1), 163–200. https://doi.org/10.1111/j.1365-246X.1975.tb00631.x

Fowler, C. M. R. (2005). *The Solid Earth: An Introduction to Global Geophysics*. Cambridge University Press.

Funiciello, F., Faccenna, C., Giardini, D., & Regenauer-Lieb, K. (2003). Dynamics of retreating slabs: 2. Insights from three-dimensional laboratory experiments. *Journal of Geophysical Research: Solid Earth*, *108*(B4). https://doi.org/10.1029/2001JB000896

Garel, F., Goes, S., Davies, D. R., Davies, J. H., Kramer, S. C., & Wilson, C. R. (2014). Interaction of subducted slabs with the mantle transition-zone: A regime diagram from 2-D thermo-mechanical models with a mobile trench and an overriding plate. *Geochemistry, Geophysics, Geosystems*, *15*(5), 1739–1765. https://doi.org/10.1002/2014GC005257

Gerardi, G., Ribe, N. M., & Tackley, P. J. (2019). Plate bending, energetics of subduction and modeling of mantle convection: A boundary element approach. *Earth and Planetary Science Letters*, *515*, 47–57. https://doi.org/10.1016/j.epsl.2019.03.010

Gerya, T. V., Yuen, D. A., & Maresch, W. V. (2004). Thermomechanical modelling of slab detachment. *Earth and Planetary Science Letters*, *226*(1–2), 101–116. https://doi.org/10.1016/j.epsl.2004.07.022

Guilmette, C., Smit, M. A., Hinsbergen, D. J. J. van, Gürer, D., Corfu, F., Charette, B., et al. (2018). Forced subduction initiation recorded in the sole and crust of the Semail Ophiolite of Oman. *Nature Geoscience*, *11*(9), 688–695. https://doi.org/10.1038/s41561-018-0209-2

Gurnis, M., Hall, C., & Lavier, L. (2004). Evolving force balance during incipient subduction. *Geochemistry, Geophysics, Geosystems*, *5*(7). https://doi.org/10.1029/2003GC000681

Hall, C. E., Gurnis, M., Sdrolias, M., Lavier, L. L., & Müller, R. D. (2003). Catastrophic initiation of subduction following forced convergence across fracture zones. *Earth and Planetary Science Letters*, *212*(1–2), 15–30. https://doi.org/10.1016/S0012-821X(03)00242-5

Iaffaldano, G. (2012). The strength of large-scale plate boundaries: Constraints from the dynamics of the Philippine Sea plate since ∼5Ma. *Earth and Planetary Science Letters*, *357–358*, 21–30. https://doi.org/10.1016/j.epsl.2012.09.018

Irvine, D. N., & Schellart, W. P. (2012). Effect of plate thickness on bending radius and energy dissipation at the subduction zone hinge. *Journal of Geophysical Research: Solid Earth*, *117*(B6), n/a-n/a. https://doi.org/10.1029/2011JB009113

Jadamec, M. A. (2015). Slab-driven Mantle Weakening and Rapid Mantle Flow. In G. Morra, D. A. Yuen, S. D. King, S.-M. Lee, & S. Stein (Eds.), *Geophysical Monograph Series* (pp. 135–155). Hoboken, NJ: John Wiley & Sons, Inc. https://doi.org/10.1002/9781118888865.ch7

Karato, S., Zhang, S., & Wenk, H.-R. (1995). Superplasticity in Earth's Lower Mantle: Evidence from Seismic Anisotropy and Rock Physics. *Science*, *270*(5235), 458–461. https://doi.org/10.1126/science.270.5235.458

Kramer, S. C., Wilson, C. R., & Davies, D. R. (2012). An implicit free surface algorithm for geodynamical simulations. *Physics of the Earth and Planetary Interiors*, *194–195*, 25–37. https://doi.org/10.1016/j.pepi.2012.01.001

MacDougall, J. G., Jadamec, M. A., & Fischer, K. M. (2017). The zone of influence of the subducting slab in the asthenospheric mantle. *Journal of Geophysical Research: Solid Earth*, *122*(8), 6599–6624. https://doi.org/10.1002/2017JB014445

McKenzie, D. P. (1977). The initiation of trenches: A finite amplitude instability. In M. Talwani & W. C. Pitman (Eds.), *Maurice Ewing Series* (Vol. 1, pp. 57–61). Washington, D. C.: American Geophysical Union. https://doi.org/10.1029/ME001p0057

Nikolaeva, K., Gerya, T. V., & Marques, F. O. (2010). Subduction initiation at passive margins: Numerical modeling. *Journal of Geophysical Research*, *115*(B3). https://doi.org/10.1029/2009JB006549

Ranalli, G., & Murphy, D. C. (1987). Rheological stratification of the lithosphere. *Tectonophysics*, *132*(4), 281–295. https://doi.org/10.1016/0040-1951(87)90348-9

Ribe, N. M. (2001). Bending and stretching of thin viscous sheets. *Journal of Fluid Mechanics*, *433*, 135–160. https://doi.org/10.1017/S0022112000003360

Schellart, W. P. (2009). Evolution of the slab bending radius and the bending dissipation in three-dimensional subduction models with a variable slab to upper mantle viscosity ratio. *Earth and Planetary Science Letters*, *288*(1–2), 309–319. https://doi.org/10.1016/j.epsl.2009.09.034

Stadler, G., Gurnis, M., Burstedde, C., Wilcox, L. C., Alisic, L., & Ghattas, O. (2010). The Dynamics of Plate Tectonics and Mantle Flow: From Local to Global Scales. *Science*, *329*(5995), 1033–1038. https://doi.org/10.1126/science.1191223

Stegman, D. R., Freeman, J., Schellart, W. P., Moresi, L., & May, D. (2006). Influence of trench width on subduction hinge retreat rates in 3-D models of slab rollback. *Geochemistry, Geophysics, Geosystems*, *7*(3), n/a-n/a. https://doi.org/10.1029/2005GC001056

Toth, J., & Gurnis, M. (1998). Dynamics of subduction initiation at preexisting fault zones. *Journal of Geophysical Research: Solid Earth*, *103*(B8), 18053–18067. https://doi.org/10.1029/98JB01076

Turcotte, D. L., & Schubert, G. (2002). *Geodynamics* (2nd ed.). Cambridge: Cambridge University Press. https://doi.org/10.1017/CBO9780511807442

van Hunen, J., & Allen, M. B. (2011). Continental collision and slab break-off: A comparison of 3-D numerical models with observations. *Earth and Planetary Science Letters*, *302*(1–2), 27–37. https://doi.org/10.1016/j.epsl.2010.11.035

Yamato, P., Husson, L., Braun, J., Loiselet, C., & Thieulot, C. (2009). Influence of surrounding plates on 3D subduction dynamics. *Geophysical Research Letters*, *36*(7), n/a-n/a. https://doi.org/10.1029/2008GL036942

Zhong, X., & Li, Z.-H. (2019). Forced Subduction Initiation at Passive Continental Margins: Velocity-Driven Versus Stress-Driven. *Geophysical Research Letters*, *46*(20), 11054–11064. https://doi.org/10.1029/2019GL084022

Table 1: Model parameters.

Quantity	**Symbol**	**Units**	**Value**
Gravity	g	m s^{-2}	9.8
Coefficient of thermal expansivity	α	K^{-1}	3×10^{-5}
Thermal diffusivity	κ	$m^2 s^{-1}$	10^{-6}
Reference density	ρ_s	kg m^{-3}	3300
Cold, surface temperature	T_s	K	273
Hot, mantle temperature	T_m	K	1573
Gas constant	R	J K^{-1} mol^{-1}	8.3145
Maximum viscosity	η_{max}	Pa s	10^{25}
Minimum viscosity	η_{min}	Pa s	10^{18}
Weak zone viscosity cap [f]	η	Pa s	10^{20}
Diffusion Creep			
Activation energy	E	kJ mol^{-1}	300 (UM)
			200 (LM)
Activation volume	V	cm^3 mol^{-1}	4 (UM)
			1.5 (LM)
Prefactor[b]	A	Pa^{-1} s^{-1}	3.0×10^{-11} (UM)
			6.0×10^{-17} (LM, ∴ $\Delta\eta = 30$)
	n		1
Dislocation Creep (UM) [c]			
Activation energy	E	kJ mol^{-1}	540
Activation volume	V	cm^3 mol^{-1}	12
Prefactor	A	Pa^{-n} s^{-1}	5.0×10^{-16}

	n		3.5
Peierls Creep (UM)[c]			
Activation energy	E	kJ mol^{-1}	540
Activation volume	V	cm^3 mol^{-1}	10
Prefactor	A	Pa^{-n} s^{-1}	10^{-150}
	n		20
Yield Strength Law			
Surface yield strength	τ_s	MPa	2
Friction coefficient	f_c		0.2[d]
	$f_{c,\ weak}$		0.02 (weak layer)[f]
Maximum yield strength	$\tau_{y,\ max}$	MPa	10,000[e]

A. UM and LM are acronyms for "upper mantle" and "lower mantle," respectively.
B. We use a generic prefactor with no explicit dependency on water content and grain size, assumed constant in the model.
C. To reduce non-Newtonian creep in the lower mantle, and upper mantle in additional cases, we set minute prefactors of 10^{-42} and 10^{-300} for dislocation and Peierls creeps, respectively.
D. A friction coefficient of 0.2 is intermediate between lower values of previous subduction models [*Di Giuseppe et al*., 2008; *Crameri et al*., *2012*] and the actual friction coefficient of the Byerlee law [*Byerlee, 1978*].
E. A very high value is taken for cases with Peierls mechanism, for which the yield mechanism dominates only at shallow depth.
F. Modified in additional cases.

Table 2: Table of cases, where plate age and geometry were changed, cases with a Y denote subducting cases and N denote failed subduction cases. The transition time represents either: (a) the transition incipient to successful subduction in subducting cases; or (b) the point at which the proportion of lithospheric viscous dissipation exceeds the lithospheric potential energy release rate in failed subduction cases.

Case Name	**Subduction**	**SP Age (Myr)**	**OP Age (Myr)**	**Bending Radius (km)**	**Bending Angle (°)**	**Initial Depth below surface (km)**	**Transition Time (Myr)**	**Modifications**
20-20Y	Y	20	20	200	77	166	8[a]	-

20-20N	N	20	20	200	67.5	141	10.5[b]	-
20-100Y	Y	20	100	200	77	166	10[a]	-
20-100N	N	20	100	200	67.5	141	10[b]	-
100-100Y	Y	100	100	200	67.5	162	20[a]	-
100-100N	N	100	100	250	45	145	6[b]	-
100-20Y	Y	100	20	200	67.5	162	-	-
100-20N	N	100	20	250	45	145	20[b]	-
65-40Y	Y	65	40	190	77	185	12[a]	-
65-40N	N	65	40	200	67.5	154	20[b]	-
40-65Y	Y	40	65	170	77	150	12[a]	
40-65N	N	40	65	140	77	124	12[b]	
LS-20-100Y-200	Y	20	100	200	77	166	7[a]	WZ = $5x10^{19}$ Pa s
LS-20-100Y-150	Y	20	100	150	77	125	15[a]	WZ = $5x10^{19}$ Pa s
LS-20-100N-125	N	20	100	125	77	104	5[b]	WZ = $5x10^{19}$ Pa s
HS-20-100N-225	N	20	100	225	77	202	-	WZ = 3 x 10^{20} Pa s

NP-65-40Y-275	Y	65	40	275	77	246	2.5[a]	No Peierls Creep
NP-65-40Y-250	Y	65	40	250	77	220	2.5[a]	No Peierls Creep
NP-65-40Y-225	N	65	40	225	77	202	18[b]	No Peierls Creep

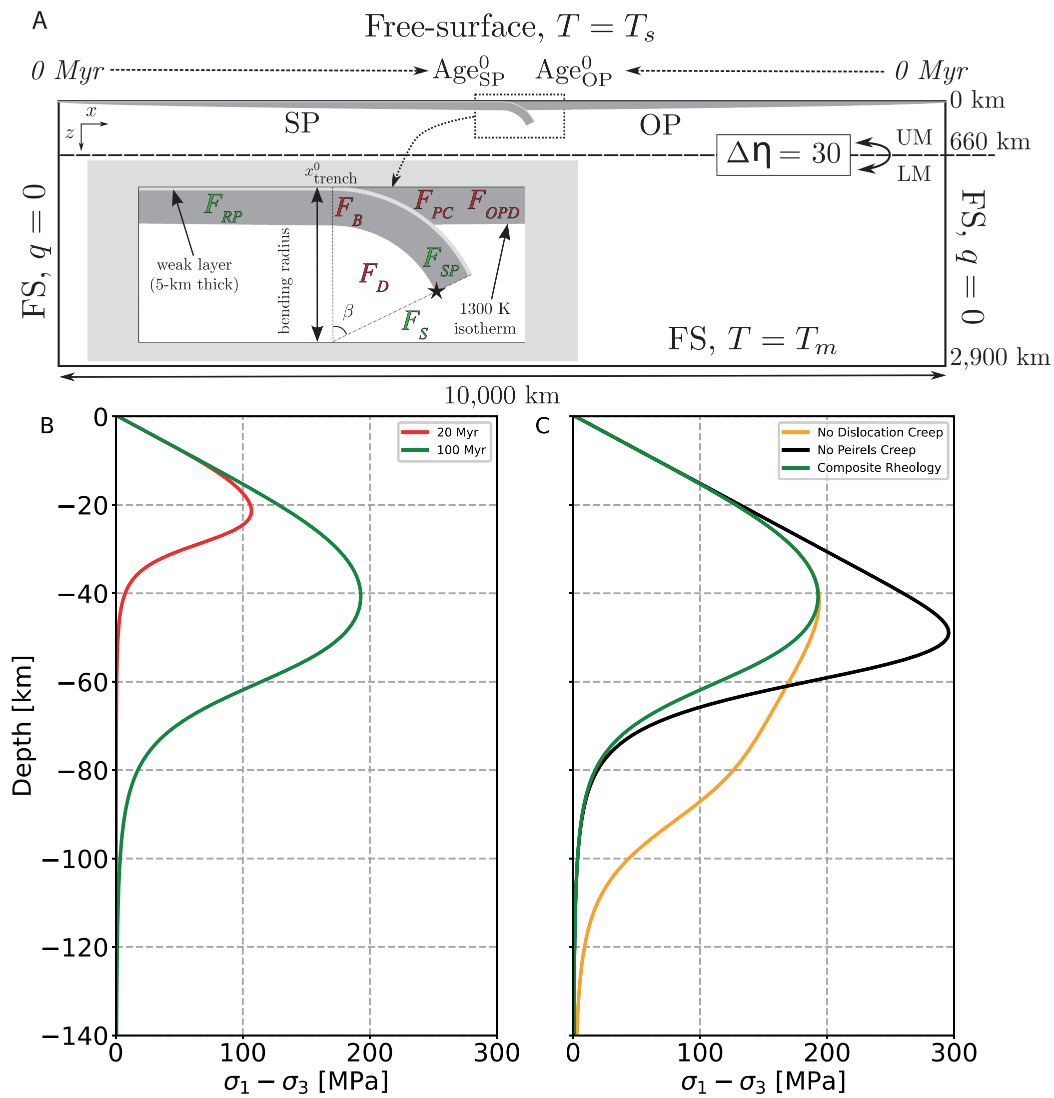

Fig. 1: A) Initial model setup, modified from Garel et al. [2014]. No rheological distinction is made between slab and upper mantle. Heat flux, q, is 0 at the side boundaries. Free-slip (FS) boundary conditions are imposed on the bottom and sides, with a free surface along the top. Age^0_{SP} and Age^0_{OP} are the initial ages of the subducting (SP) and overriding plates (OP) at the trench, respectively. $\Delta\eta = 30$ is the jump between diffusion creep upper (UM) and lower mantle (LM) viscosity at 660 km. The initial hook geometry of the subducting plate is prescribed using a variation in bending radius (including the weak layer, shown in light grey) and β. The star indicates the location at which the initial slab tip depths have been measured. The driving forces (green) – Ridge push (F_{RP}), slab pull (F_{SP}) and suction due to slab break-off (F_S) as well as resisting forces (red) – bending (F_B), mantle drag (F_D) plate coupling (F_{PC}) and over-riding plate deformation (F_{OPD}) are included. Modified from Garel et al. [2014]. B) Initial strength profiles using a composite rheology and a background strain rate of 10^{-15} s^{-1} of a 20 Myr and 100 Myr slab at the trench. C) Initial strength profiles of a 100 Myr slab at the trench with a composite rheology, or with dislocation or Peirels creep removed and a background strain rate of 10^{-15} s^{-1}.

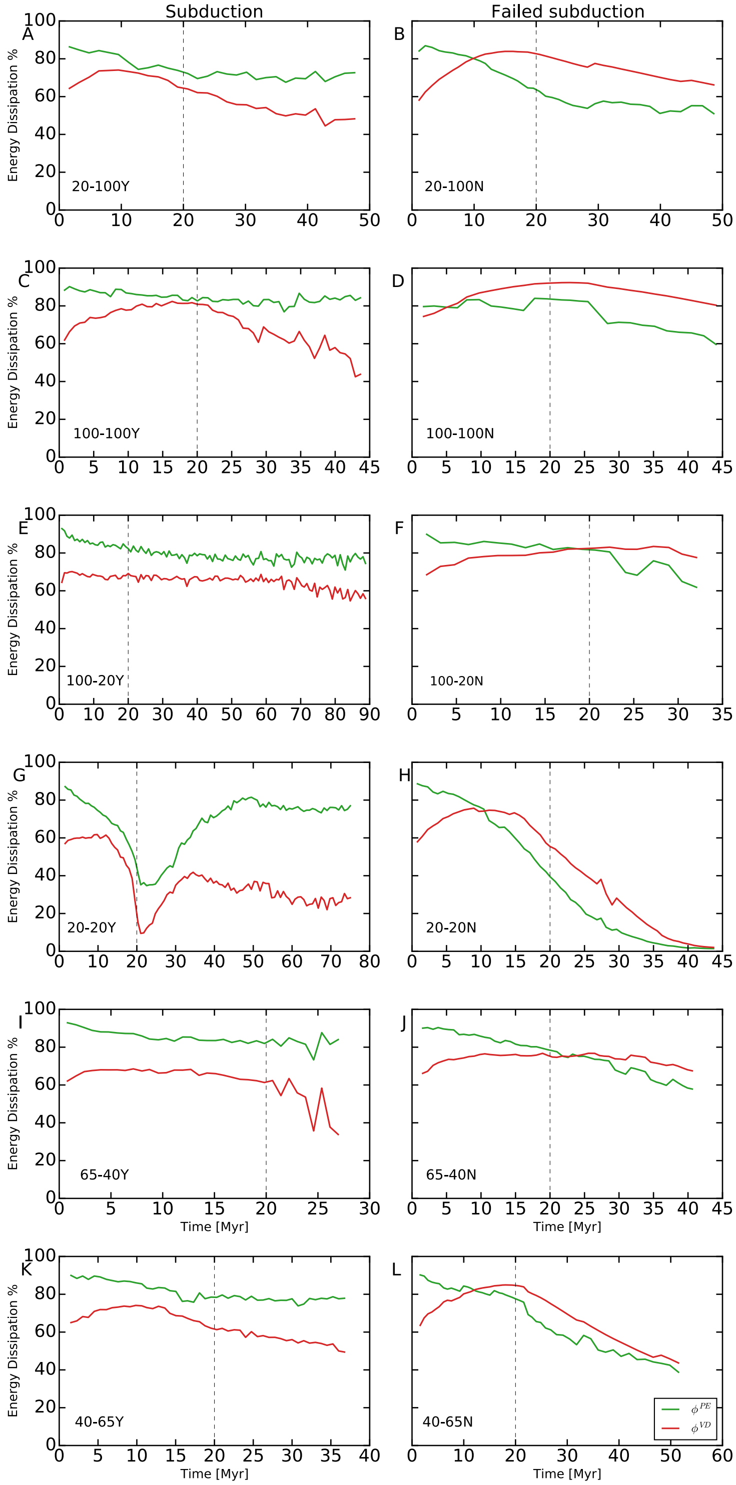

Fig. 2: Evolution of dissipation of lithospheric potential energy release rate and viscous dissipation for each model, case numbers are included in the panel. The red line represents the percentage of lithospheric viscous dissipation in the model (ϕ^{VD}) whilst the green line represents

the percentage of lithospheric potential energy release rate (ϕ^{PE}). The dotted line represents 20 Myr in the evolution, the critical duration of the incipient stage. All failed cases have ϕ^{PE} decrease below ϕ^{VD} within 20 Myr, which is not observed in successful cases.

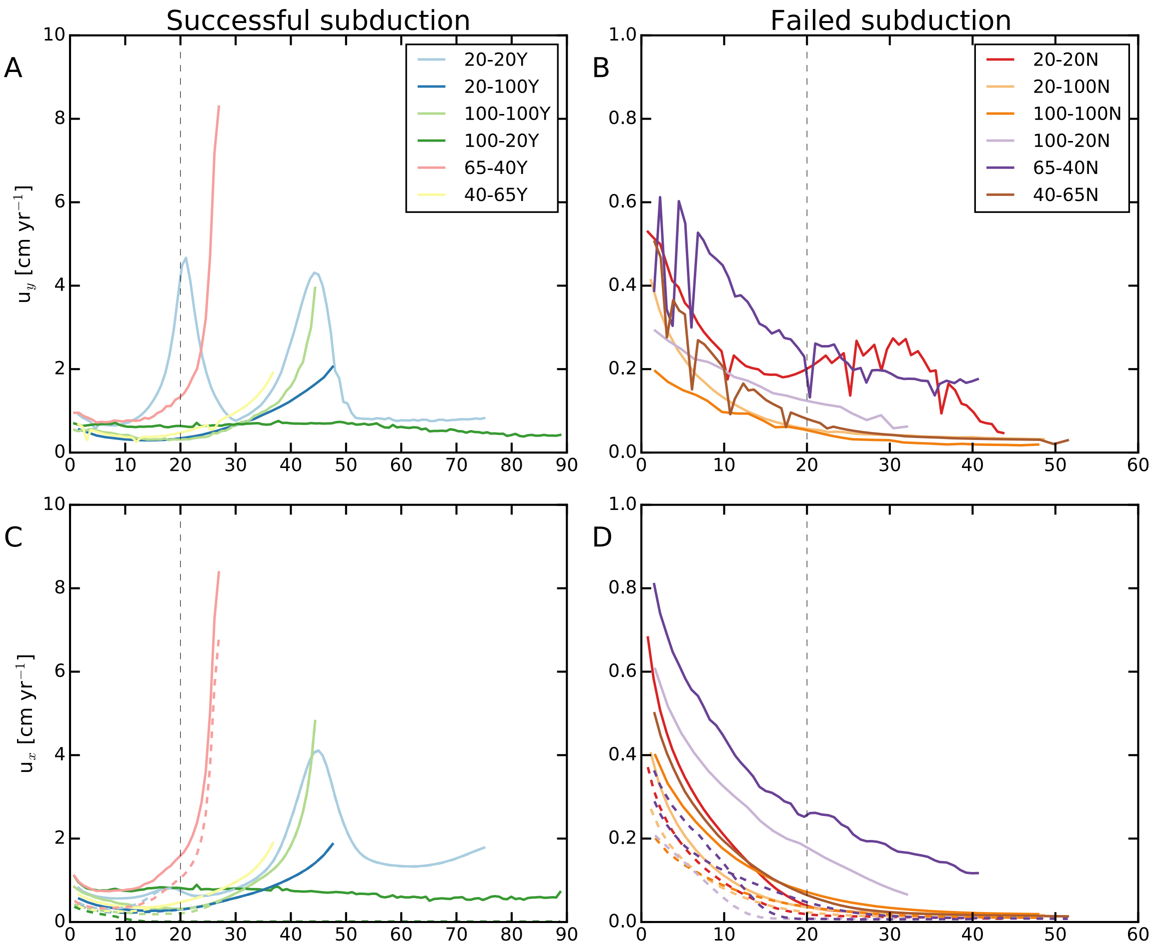

Fig. 3: A) Vertical velocity (u_y) of the slab tip of successful subducting cases. B) Vertical velocity (u_y) of the slab tip of failed subduction cases. C) Convergence velocity (u_x - solid) and subducting plate horizontal velocity (u_{sp} - dashed) of successful cases. D) Convergence velocity (u_x - solid) and subducting plate horizontal velocity (u_{sp} dashed) of failed cases. All Subducting cases have a minimum convergent velocity of ~ 0.5 cm yr^{-1}, whilst all failed cases tend toward 0 cm yr^{-1}.

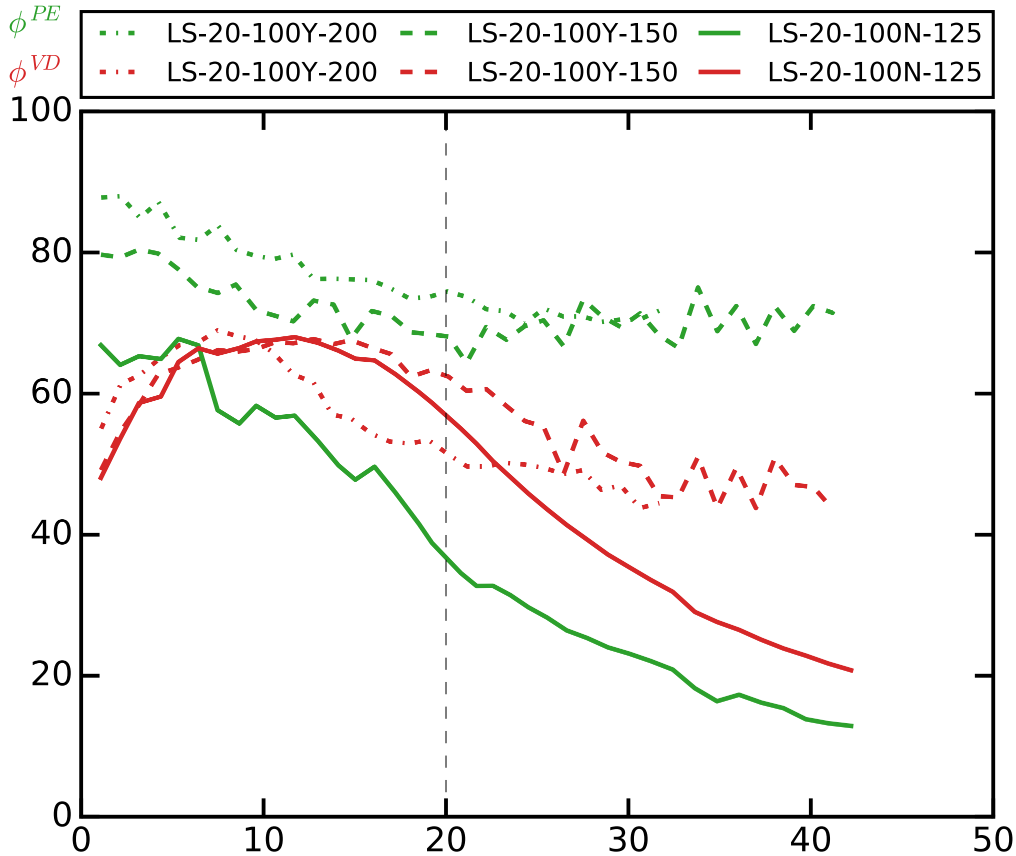

Fig. 4: Energy dissipation when a viscosity cap of 5 x 10^{19} Pa s is applied to the weak zone, with varying bending radius (BR), and thus initial slab tip depth below surface (IDBS), for cases LS-20-100Y-200, LS-20-100Y-150 and LS-20-100N-125 (BR – 200, 150, 125 km, IDBS – 166, 125, 104 km, respectively). The results suggest that subduction reaches a successful for a bending radius of > 150 km (LS-20-100Y-150) or an initial slab tip depth of 125 km. The results also show that with an increasing slab length, the lithospheric strength is easier to over-come and the duration of the incipient stage is shorter due to the slabs higher potential energy.

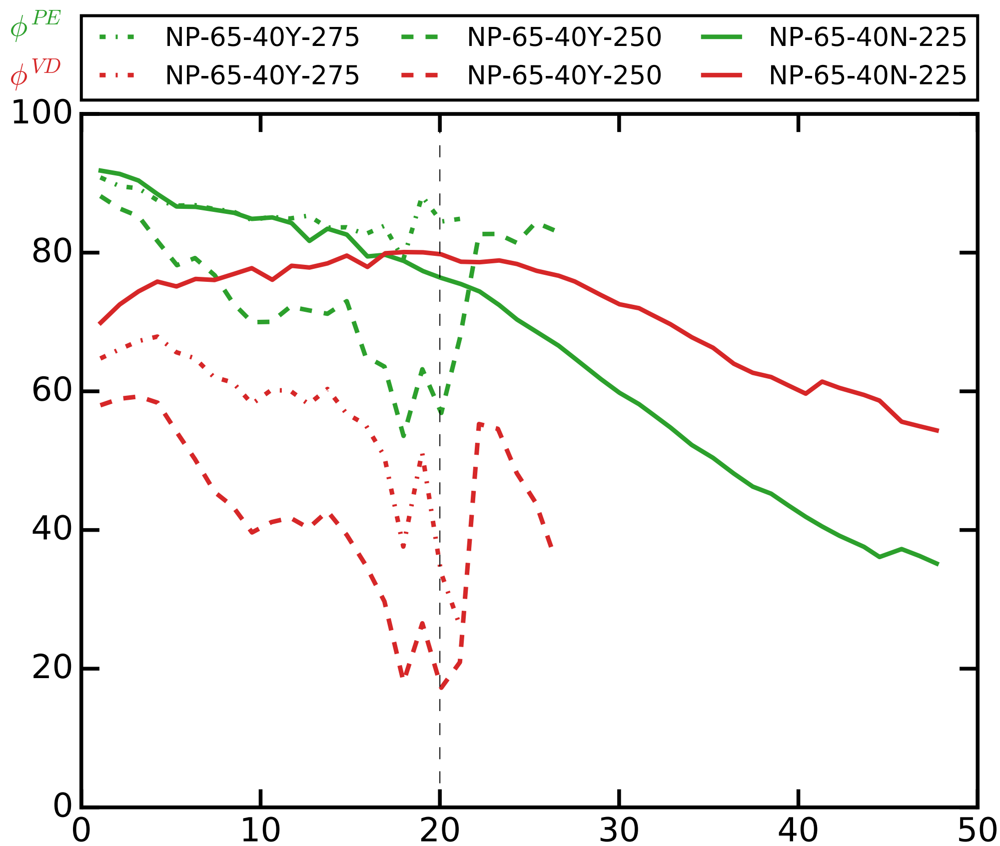

Fig. 5: Energy dissipation of the case without the Peierls creep deformation mechanism, with varying bending radius (BR), and thus initial slab tip depth (IDBS), for cases NP-65-40Y-275, NP-65-40Y-250 and NP-65-40N-225 (BR – 275, 250, 225 km, IDBS – 246, 220, 202 km, respectively). The results show an initial BR of 250 km (depth of >220km, case 65-40Y-B) is required for subduction to reach a successful state. In these cases, the lithospheric viscous dissipation peaks early and transitions to mantle dominated as the slab remains strong and the mantle is preferentially deformed due to the removal of the Peierls creep deformation mechanism.

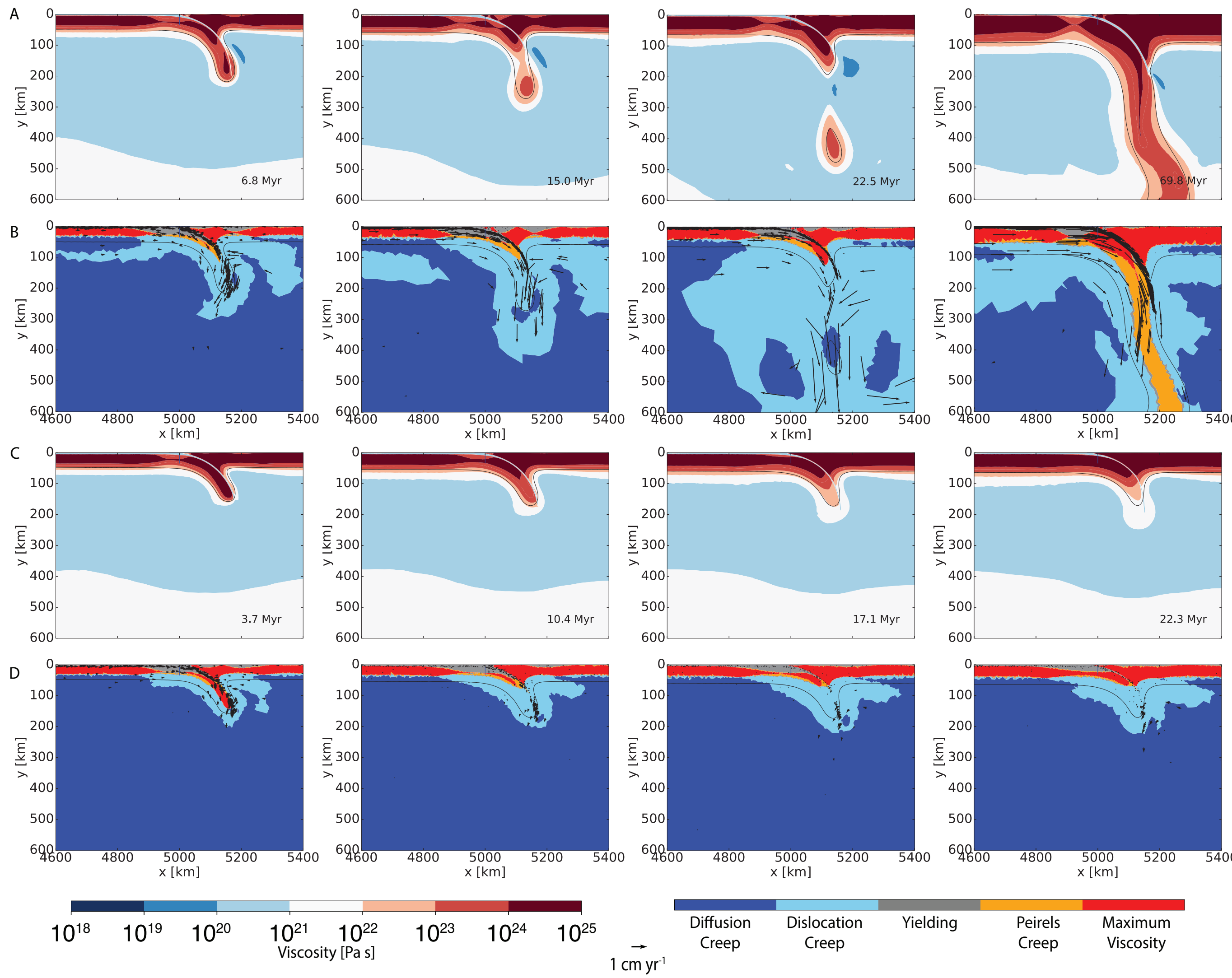

Fig. 6: Evolution of case 20-20Y showing a) Viscosity and b) main deformation mechanism with velocity vectors and 20-20N showing c) Viscosity and d) main deformation mechanism with velocity vectors. The effect of slab break-off is seen clearly in the mantle where lower levels of viscosity and suction, highlighted by the velocity vectors, are caused by the broken portion of the slab as it sinks freely in the upper mantle. Case 20-20N shows how the slab thermally diffuses away over 20 Myr.

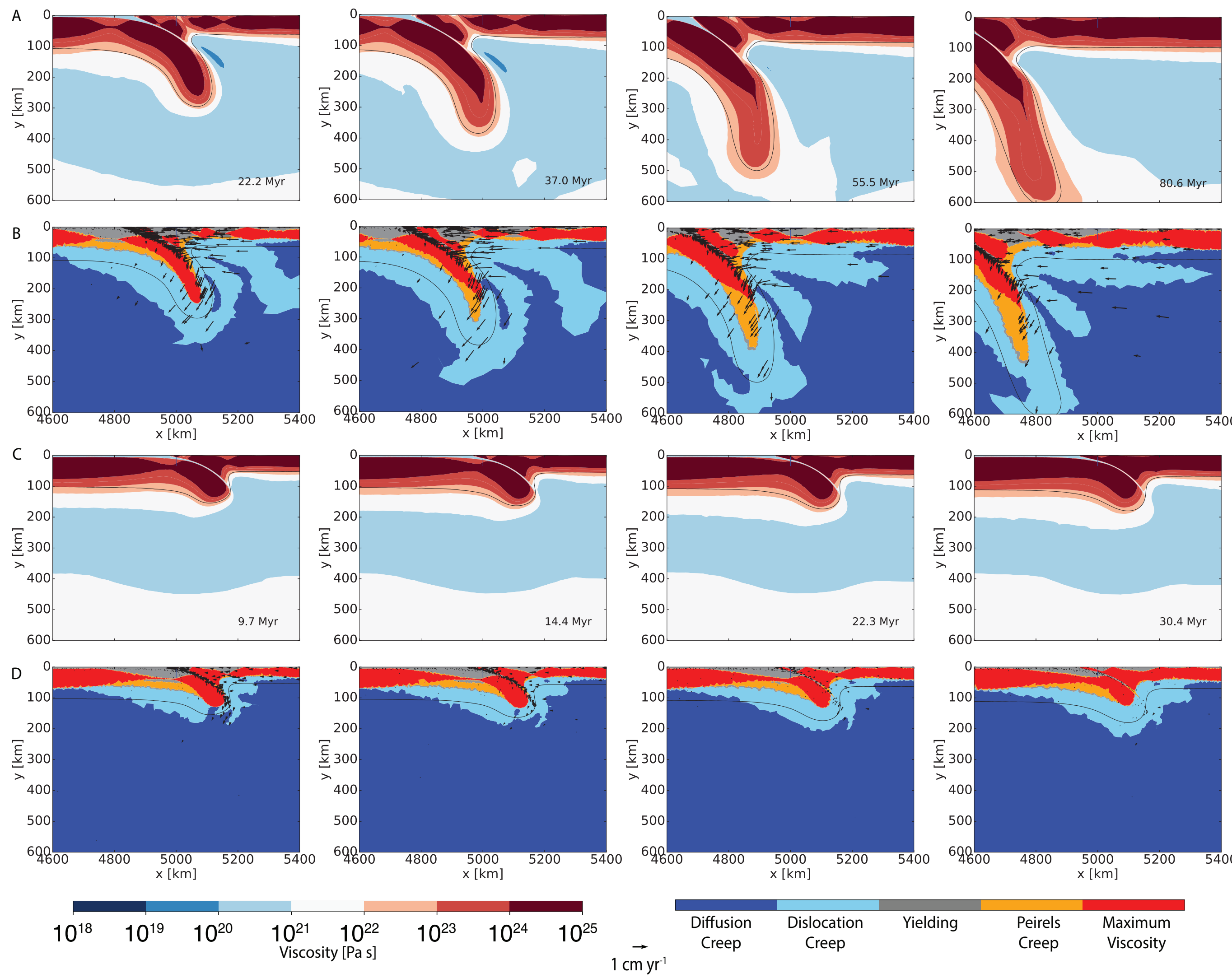

Fig. 7: Evolution of case 100-20Y, showing a) Viscosity and b) main deformation mechanism and velocity vectors and case 100-20N, showing c) Viscosity and d) main deformation mechanism and velocity vectors. The evolution of case 100-20Y demonstrates the deformation and reduced strength in the over-riding plate caused by slab roll-back, and the subducting plate remains rigid. 100-20N shows how the slab thermally diffuses away over 20 Myr.

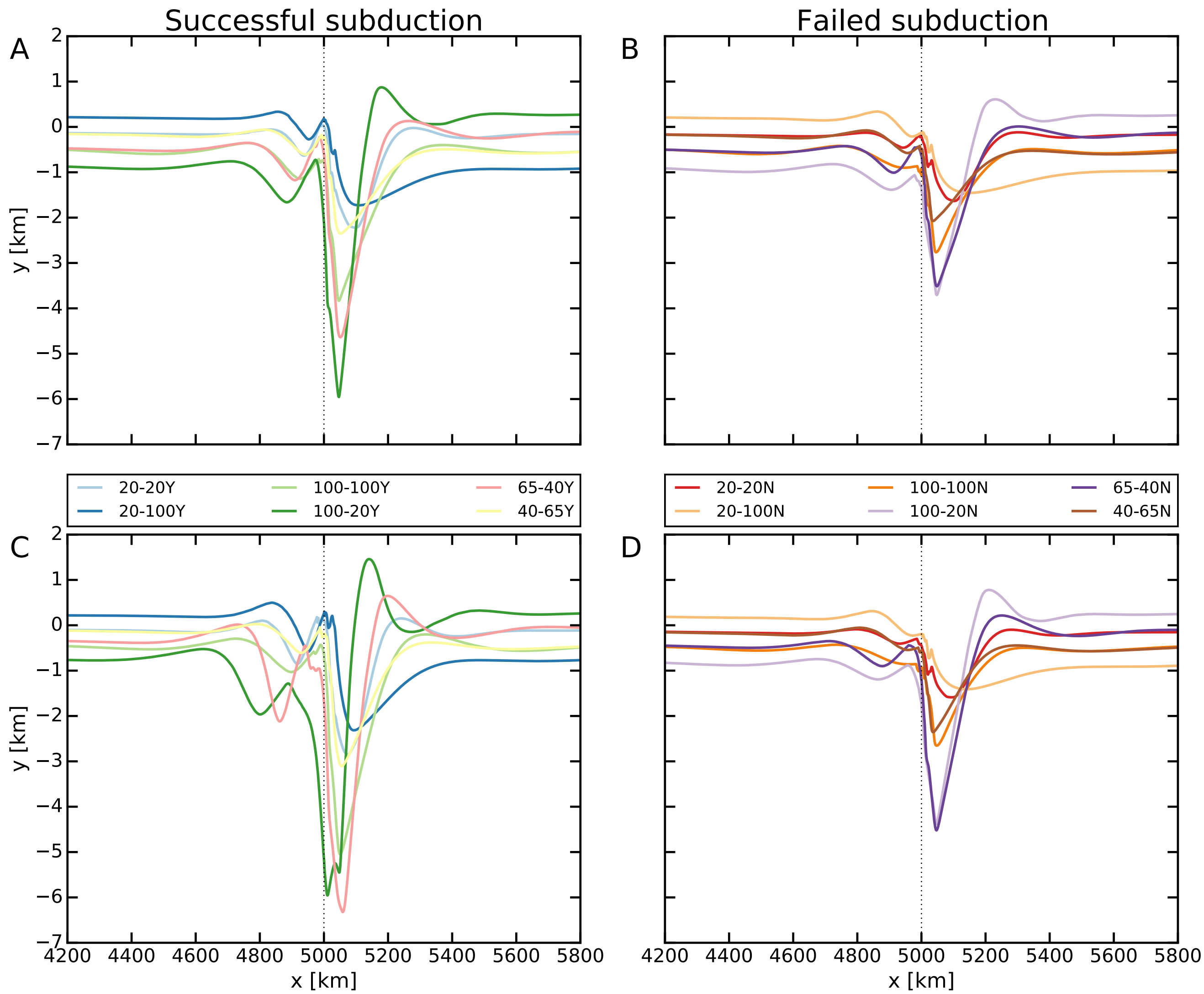

Fig. 8: Free surface heights for each case, representing topography. A) Free surface after 5 Myr for successful cases, with the development of topographic features. B) Failed cases after 5 Myr, development of some topography, but does not develop further. C) Subducting cases, with larger extremes in free surface height associated with older subducting slabs, however the wavelength of each feature remains fairly consistent across a range of plate ages. D) Failed subduction cases, with the trench still clearly visible in each case.

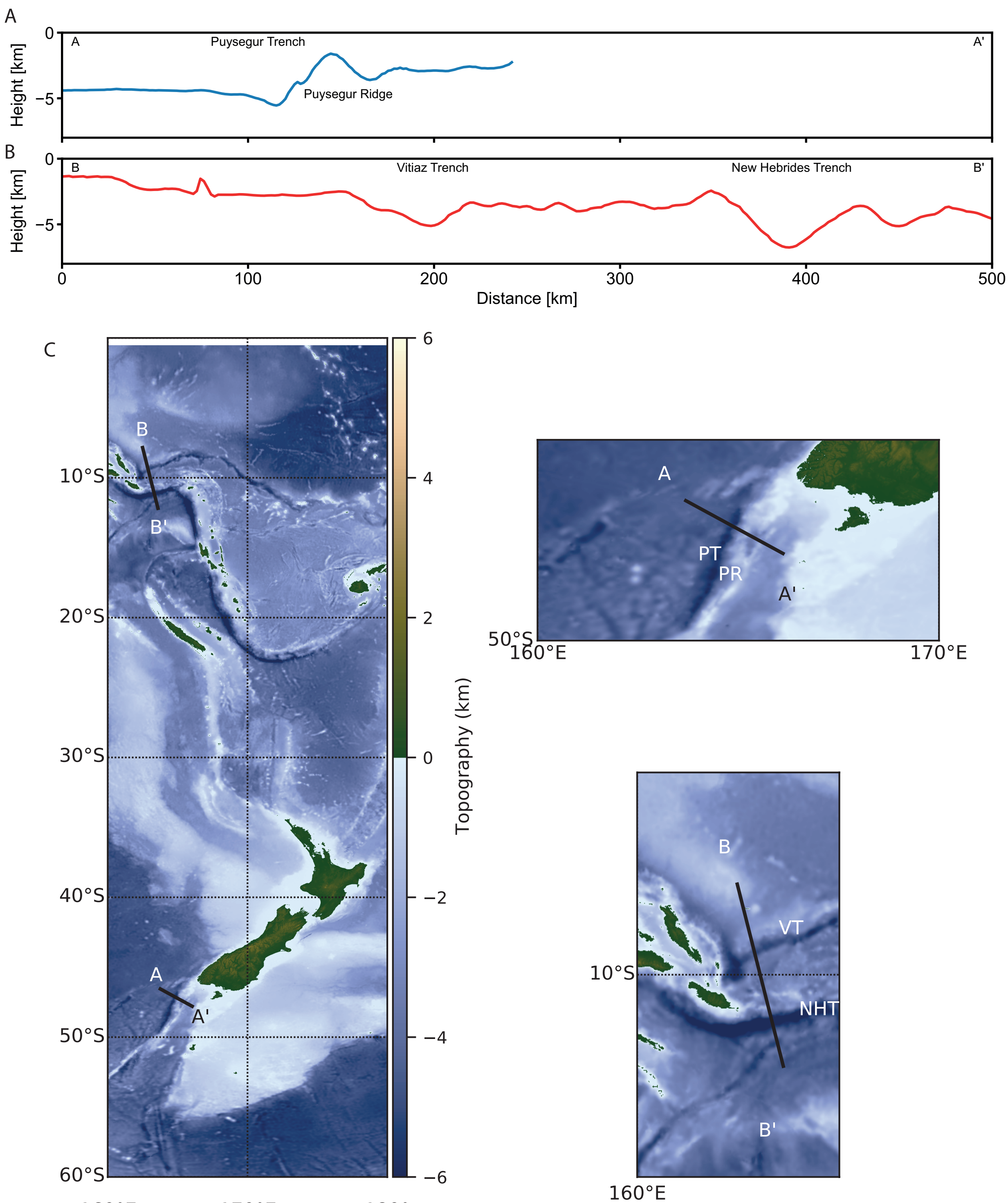

Fig. 9: A) Topography across the Psysegur subduction zone. B) Topography across the Vitiaz (VT) and New Hebrides (NH) trenches. C) Topographic data from etopo1 [Amante and Eakins, 2009].